Fatigue & Fracture of Engineering Materials & Structures

WILEY

FFEMS Fatigue & Fracture of Engineering Materials & Structures

ORIGINAL ARTICLE OPEN ACCESS

Crack Arrest Analysis of Components With Compressive Residual Stress

Xuran Xiao[1] | Volodymyr Okorokov[2] | Donald Mackenzie[1]

[1]Department of Mechanical & Aerospace Engineering, University of Strathclyde, Glasgow, UK | [2]Department is Mechanical & Aerospace Engineering, Weir Minerals Netherlands, Venlo, Netherlands

Correspondence: Xuran Xiao (xuran.xiao.2017@uni.strath.ac.uk)

Received: 30 April 2024 | **Revised:** 11 November 2024 | **Accepted:** 1 December 2024

Keywords: 3D finite element analysis | crack arrest | crack propagation | residual stress

ABSTRACT

A finite element analysis and fracture mechanics methodology for determining the autofrettage pressure required to cause crack arrest in components under varying pressure loading are presented. Superposition of the autofrettage residual stress distribution and working load stress distribution is combined with ANSYS Separating Morphing and Adaptive Remeshing Technology (SMART) to determine the effective stress intensity factor as the crack grows. The condition for crack arrest is identified by comparison with a crack arrest model defining the crack propagation threshold stress intensity factor range for microstructurally short, physically short, and long cracks. The crack propagation threshold models of El Haddad and Chapetti are implemented and applied to fatigue analysis of stainless steel and low carbon steel double notch tensile test specimens with preinduced compressive residual stress. Based on comparison with fatigue test results, the Chapetti model is selected for use in the analysis of a 3D aluminum alloy valve body. The calculated minimum autofrettage pressure required to give crack arrest under a given working load cycle is found to be in good agreement with experimental observations from the literature.

1 | Introduction

The fatigue life of components subject to repeated or cyclic loading can be enhanced by inducing compressive residual stress in regions prone to fatigue crack initiation and propagation. This can be achieved through several different mechanical processes, such as shot peening, laser peening, low plasticity burnishing, swaging [1–4], and autofrettage [5–8]. These processes result in a self-equilibrating residual stress system in the component at zero load, with compressive residual stress at critical locations. The resulting increase in fatigue life can be determined by several approaches, including stress life analysis and fatigue life assessment based on fracture mechanics.

In stress life analysis, the fatigue life of a component is assessed through linear elastic stress analysis and reference to experimental fatigue life data in the form of SN (stress number of cycles to failure) curves. Fatigue life is usually determined by the stress cycle at a local stress raising feature. Residual compressive stress induced in these regions prior to installation has the effect of reducing the local mean stress under working loads. Depending on the compressive stress magnitude, applying mean stress correction may indicate an increased number of cycles to failure, or even theoretical infinite life if the resulting stress cycle is below the material endurance limit.

In fracture mechanics analysis, the magnitude and distribution of the compressive residual stress may prevent crack initiation,

Summary

- A procedure to determine autofrettage pressure based on crack arrest analysis is presented.
- Two crack propagation threshold models were considered.
- Finite element analysis of induced residual stress and crack growth is shown.
- Analysis results show good agreement with available experimental results.

resulting in theoretical infinite fatigue life. Alternatively, crack initiation may be prolonged and crack growth either retarded due to crack closure effects, increasing the number of cycles to failure, or arrested by the compressive residual stress field, resulting in a theoretical infinite fatigue life.

This paper considers hydraulic autofrettage of pressure retaining components or vessels subject to variable loading in the high cycle fatigue range. In hydraulic autofrettage, the component is subject to internal pressure great enough to cause limited plastic deformation in highly loaded regions prior to service. When this autofrettage pressure is reduced to zero, the elastically deformed regions of the vessel seek to recover their original dimensions but are prevented from doing so by the permanent deformation of the plastically deformed material, inducing residual compressive stress at these locations. Numerical modeling of autofrettage involves both the loading and unloading processes. Typically, a structure is subjected to internal pressure that causes yield and upon unloading, multiaxial residual stress is induced to increase the fatigue strength [9, 10]. Experimental investigations have shown that this procedure can significantly increase the fatigue life of components or vessels in subsequent operation. Mughrabi et al. found the fatigue limit can be increased by more than 40% by autofrettage [11]. Other autofrettage studies by Rees, Parker and Underwood, Badr et al., Lee and Koh, Pölzl and Schedelmaier, Thumser et al. and Sellen et al. have reported fatigue strength increase greater than 60% [12–18]. Jahed et al. found that the fatigue life after autofrettage was increased by a factor of 2.11 [19].

From a design perspective, the aim of autofrettage for a given working load cycle may be to achieve a specific finite fatigue life, typically 10^6 to 10^7 cycles for high cycle fatigue, or theoretical infinite fatigue life. The minimum autofrettage pressure required to achieve this aim can be determined by applying a stress life, a strain life, or a fracture mechanics methodology [20] to a component with induced compressive residual stress calculated by elastic–plastic analysis.

The stress life approach is applied to the component to calculate the fatigue life for several different autofrettage pressures [21] to establish the minimum value meeting the design requirement. In components with local stress raisers, or notches, this approach is complicated by the stress gradient at the notch, which is influenced by both the notch and the residual stress distribution [7]. For notched components, the theory of critical distance approach is widely used to calculate an "average" stress amplitude over the critical distance, based on a constant stress ratio, to predict the fatigue life or limit. However, with induced residual stress, the varying stress ratio means that this approach is not directly applicable [22].

The fracture mechanics approach requires a model for crack initiation and a model for crack propagation. Modeling crack propagation in a varying residual stress field is complicated by a variation in crack tip stress ratio as the crack grows. The influence of residual stress may be characterized by defining a stress intensity factor (SIF) for the residual stress, K_{rs}. This can be achieved through application of a weight function method, such as the following [23]:

$$K_{rs} = \int_{x=0}^{x=a} \sigma_{rs} m(x,a) dx \tag{1}$$

where, a is the crack length, σ_{rs} is the residual stress, and $m(x,a)$ is the weight function. The weight function is determined by considering individual constant and linear crack face pressure fields [24]. The SIF for each pressure field is calculated and combined to determine the weight function for calculating the SIF corresponding to the residual stress distribution. However, this approach can be problematic for complex 3D structures such as pressure vessels, pumps, and valves [6]. In previous work [25], the present writers proposed an alternative method for modeling high cycle fatigue crack propagation, combining superposition of applied load and residual stress fields [26] with ANSYS Separating Morphing and Adaptive Remeshing Technology (SMART) technology [27–29]. Compared to the traditional extended finite element method (XFEM), the SMART crack growth method reduces computational time by using the unstructured mesh method (UMM), which allows for remeshing the crack front instead of splitting volume elements as in XFEM. Additionally, the SMART tool incorporates the interaction integral method [30] to calculate the decoupled SIFs. One of the limitations of SMART crack growth is that only linear elastic fracture mechanics (LEFM) is supported, but the establishment of residual stress requires plastic deformation. Therefore, the superposition method proposed in previous work [31] is used to calculate K_{rs} and predict the fatigue life. However, the method does not account for the possibility of crack arrest and consequent theoretical infinite fatigue life. This paper investigates incorporation of the crack arrest models of El Haddad et al. [32] and Chapetti [33] in the methodology. Both models are initially investigated in fatigue analysis of double notch tensile test specimens with compressive residual stress induced by initial tensile overload. Results are compared with fatigue test results from the literature and additional results not previously presented. The procedure with the Chapetti crack arrest model is then applied to a complex 3D valve body with autofrettage residual stress, previously considered by Sellen et al. [34].

2 | Methodology

The analysis procedure adapted from the previous work [25] is described schematically in Figure 1. Three models for the finite element analysis (FEA) are used.

The first stage in the analysis is to determine the residual stress distribution in the component after autofrettage. This is done

using FEA Model 1, which has an elastic–plastic material model based on monotonic stress–strain data. The calculated residual stress distribution is then exported as an initial stress state to two other finite element models.

Model 2 is an elastic–plastic model based on a cyclic stress–strain curve. This is used to calculate the stress amplitude, σ_a, resulting from the combined applied pressure and residual stress. Mean stress correction is applied to determine the equivalent stress amplitude, σ_{ar}. Crack initiation is assumed to occur at the maximum σ_{ar} location.

Model 3 is used to analyze crack propagation from the crack initiation location from Model 2, using the ANSYS SMART crack growth tool calculate variation in SIF range with increasing crack length a. This can be done for components with and without autofrettage. When autofrettage is considered, the calculated residual stress distribution from Model 1 is imported as an initial stress state. SMART automatically models crack propagation, remeshing the crack tip region and calculating stress redistribution and SIFs as the crack grows.

A superposition method is then applied to calculate the SIF range for the applied pressure, ΔK_{app} and the residual stress SIF, K_{rs}, from which the effective SIF range, ΔK_{eff}, is calculated. The calculated effective SIF range is then compared with a crack threshold model to determine if the crack will propagate or will be arrested. The autofrettage pressure at which crack arrest occurs can be determined by repeating the procedure for several autofrettage and applied pressure values.

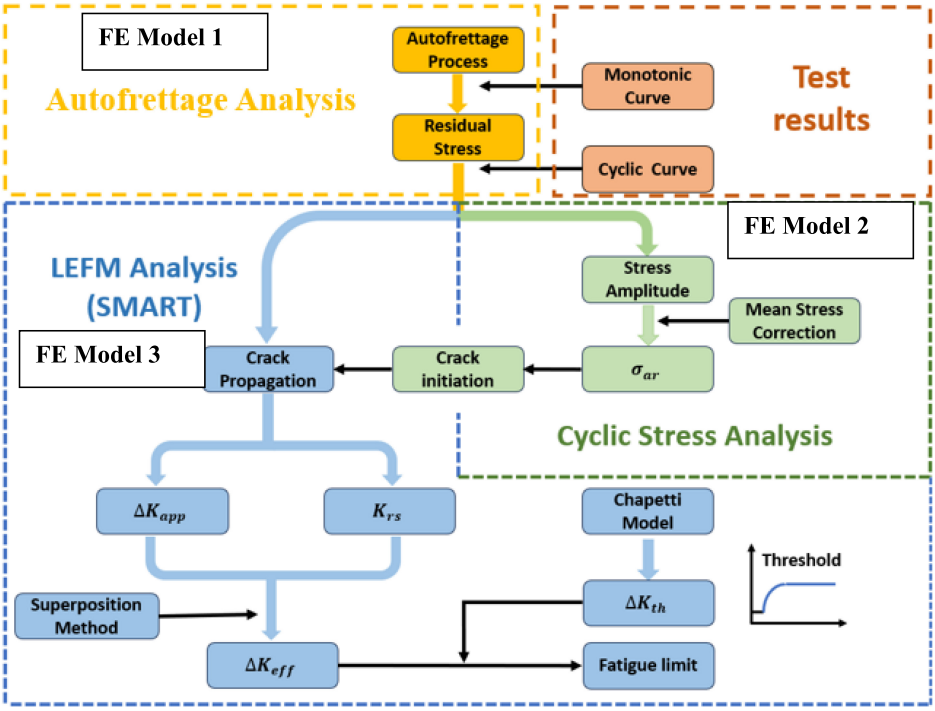

FIGURE 1 | Flow diagram of analysis methodology. [Colour figure can be viewed at wileyonlinelibrary.com]

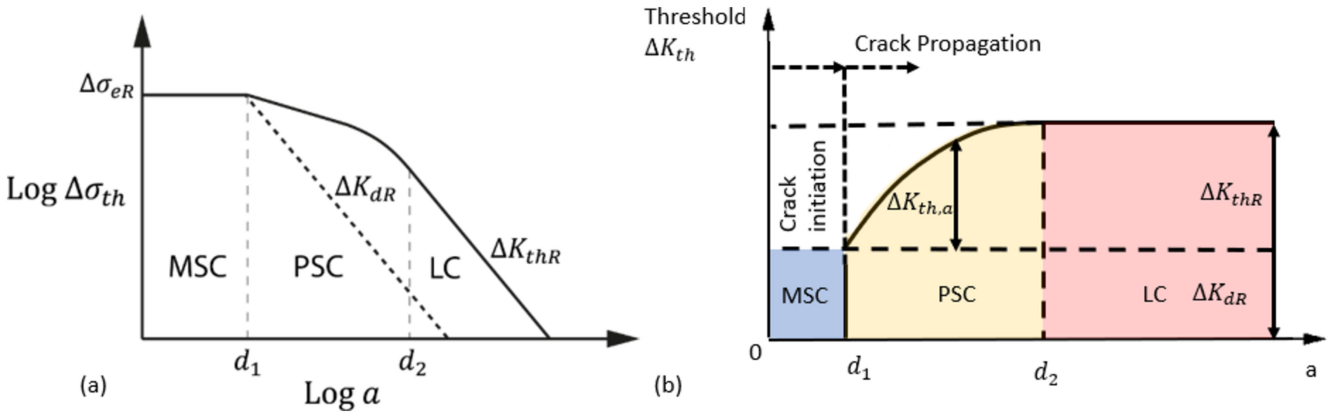

FIGURE 2 | (a) Schematic Kitagawa–Takahashi (KT) diagram. (b) Variation of threshold of stress intensity factor range with crack size. [Colour figure can be viewed at wileyonlinelibrary.com]

3 | Crack Arrest Models

In stress life analysis, the fatigue or endurance limit stress range $\Delta\sigma_{th}$ defines a stress cycle below which fatigue cracks do not propagate. In fracture mechanics, a fatigue crack propagation threshold defines a SIF range ΔK_{th} below which existing cracks will not propagate. The two thresholds are related by the expression:

$$\Delta K_{th} = Y\,\Delta\sigma_{th}\sqrt{\pi a} \tag{2}$$

where Y is a geometrical configuration factor and a is the crack length. The schematic Kitagawa–Takahashi (KT) diagram [35] of Figure 2a illustrates the relationship between $\Delta\sigma_{th}$ and a for microstructurally short cracks (MSCs), physically short cracks (PSCs), and long cracks (LC) for a fixed stress ratio R. Length d_1 and d_2 are characteristic microstructural dimensions that identify the transitions between MSC and PSC and between PSC and LC, respectively.

For an MSC of length $a \le d_1$, crack propagation will occur if the applied stress range is greater than or equal to the plain fatigue limit range $\Delta\sigma_{eR}$. Below this value, cracks are arrested at microstructural barriers. For a LC $a \ge d_2$, propagation will occur when the SIF range is greater than the threshold value ΔK_{thR}.

El Haddad et al. [32] proposed the threshold SIF range for a PSC of length a, $\Delta K_{th,a}$, as

$$\Delta K_{th,a} = \Delta K_{thR}\sqrt{\frac{a}{d_2}} \tag{3}$$

where the value of d_2 for an edge short crack can be determined from ΔK_{thR} and fatigue limit σ_f as [36]

$$\Delta K_{thR} = 1.12\sigma_f\sqrt{\pi d_2}. \tag{4}$$

Chapetti [33] proposed an alternative model in which the PSC threshold SIF range has intrinsic and extrinsic components. The intrinsic threshold ΔK_{dR} is dependent on the plain fatigue limit and characteristic dimension d_1:

$$\Delta K_{dR} = Y\,\Delta\sigma_{eR}\sqrt{\pi d_1}. \tag{5}$$

In the extrinsic component of the threshold SIF range, ΔK_{th} increases from ΔK_{dR} to ΔK_{thR}, as illustrated in Figure 2b. The threshold SIF range for a PSC of length a is defined as

$$\Delta K_{th,a} = \Delta K_{dR} + \left(\Delta K_{thR} - \Delta K_{dR}\right)\left[1 - e^{-k(a-d_1)}\right] \tag{6}$$

where k is the material constant given by

$$k = \frac{1}{4d_1}\frac{\Delta K_{dR}}{\Delta K_{thR} - \Delta K_{dR}} \tag{7}$$

When the crack length is greater than d_2, the threshold SIF range is constant at ΔK_{thR}.

Crack arrest analysis based on the El Haddad and Chapetti models have been considered in several investigations. Araújo and Nowell [36] and de Pannemaecker et al. [37] adopted the El Haddad model for crack arrest analysis in fretting fatigue. Chapetti and Jaureguizahar [38] assessed fatigue strength by comparing the threshold curve with ΔK. Chapetti assumed a semicircular crack, with $Y = 0.65$. Santus and Taylor [39] have proposed a semiellipse form where Y is dependent on aspect ratio, with $Y = 0.746$ assumed for an aspect ratio 0.8. A similar IBESS approach [40] was proposed for fatigue assessment of welding structures.

Crack arrest analysis taking account of autofrettage pressure was investigated for cruciform specimens by Thumser et al. [41] in terms of ΔK_{dR}. This applies to cracks within the MSC region, but when defining crack arrest in general, it is necessary to consider variation in the PSC threshold with a, $\Delta K_{th,a}$, as illustrated in Figure 2b. Even if ΔK exceeds ΔK_{dR}, there is still a possibility

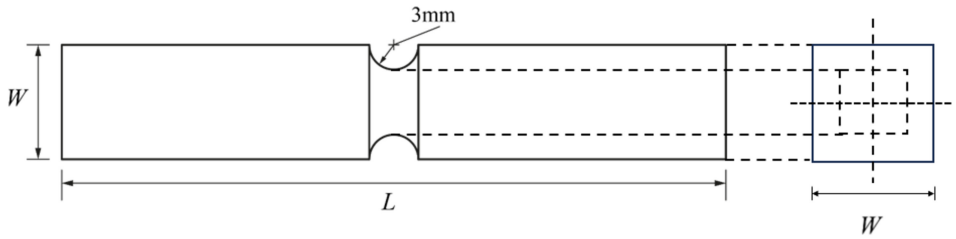

FIGURE 3 | Dimensions of double-notched specimens. [Colour figure can be viewed at wileyonlinelibrary.com]

TABLE 1 | Experimental and collected material properties of 316L and S355 ($R = 0$) [20, 22, 25, 43, 44].

Material	σ_y (MPa)	E (GPa)	$\Delta\sigma_{eR}$ (MPa)	$\Delta K_{thR}\left(\text{MPa}\sqrt{\text{m}}\right)$	d_1 (mm)	d_2 (mm)	$\Delta K_{dR}\left(\text{MPa}\sqrt{\text{m}}\right)$	$k\left(\text{mm}^{-1}\right)$
316L	255	200	292	5.5	0.024	0.36	1.64	4.46
S355	255	200	344	8	0.055	0.55	2.94	2.64

of arresting the crack due to increasing $\Delta K_{th,a}$. An alternative way to calculate crack arrest is to generate the threshold of SIF range curve (R curve) by considering the plasticity induced by crack closure [42].

4 | Double Notch Tensile Specimens

The proposed method is initially investigated for fatigue analysis of double notch tensile test specimens with induced compressive residual stress. Compressive residual stress is induced in the notched region of the specimens prior to fatigue testing by applying a tensile overload great enough to cause limited plastic deformation in the notch intersection region. When the load is removed, compressive residual stress is induced at the corners due to recovery of the elastically deformed interior material. The localized nature of the residual stress distribution is similar to that found at stress raising features in pressure components.

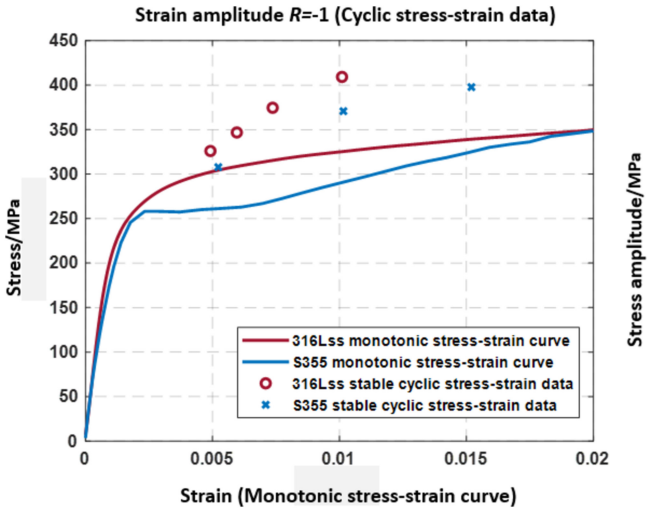

FIGURE 4 | Monotonic stress–strain curves and cyclic stress–strain data of 316Lss [25] and collected curve of S355 [22]. [Colour figure can be viewed at wileyonlinelibrary.com]

The method was applied to two types of double-notched tensile test specimens, Type A and Type B, previously investigated by the present writers [22,25]. The geometry and dimensions of the square cross-section specimens are shown in Figure 3. Specimen type A is 316L stainless steel, and specimen type B is S355 low carbon steel. For specimen type A, W is 14 mm, and $\boldsymbol{L}$ is 150 mm, and for specimen type B, W is 21 mm, and $\boldsymbol{L}$ is 180 mm.

4.1 | Material Properties

The material properties used in the FEA and crack propagation threshold models, obtained from the literature [20, 22, 25, 43, 44], are given in Table 1. For detailed elastic–plastic analysis, according to the definitions of offset strain reviewed by Abdel-Karim [45], σ_y is determined from the 0.01% proof stress, rather than the 0.2% proof stress.

Monotonic stress–strain curves and cyclic stress–strain data for 316L [25] and S355 [22] are shown in Figure 4. Multilinear kinematic model is applied to fit the monotonic curve. The Chaboche kinematic hardening material model is applied to the stable cyclic stress–strain curves, with parameters $C_1 = 63{,}400$ MPa and $\gamma_1 = 303.41$ for 316L stainless steel and $C_1 = 30{,}489$ MPa and $\gamma_1 = 135.41$ for S355 low carbon steel.

4.2 | Finite Element Models

Both specimen types were modeled in ANSYS Workbench using SOLID 187 tetrahedral structural solid elements. The three

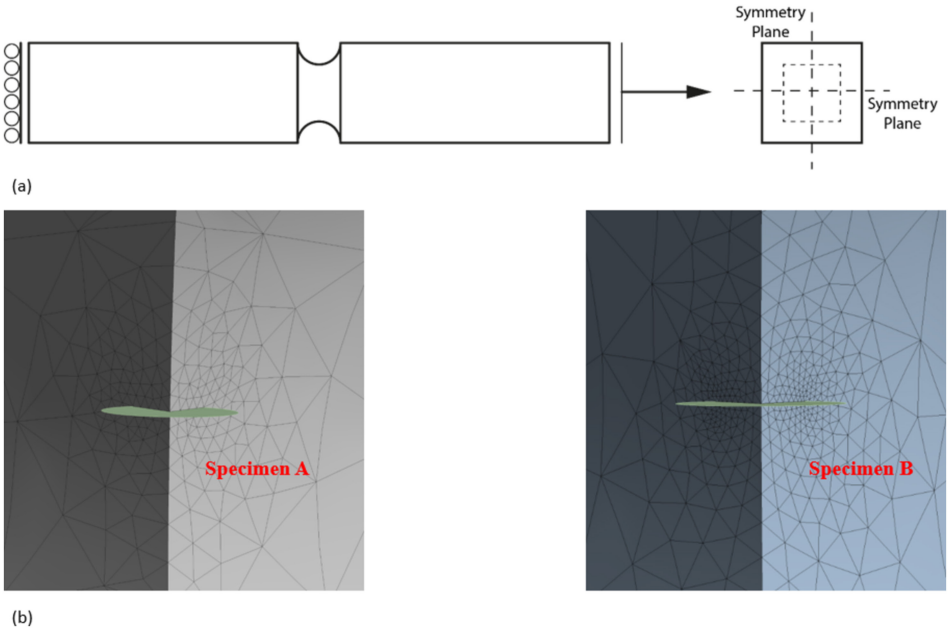

FIGURE 5 | (a) Finite element model symmetry planes and boundary conditions. (b) Finite element mesh plots in the notch regions (specimen type A 316L stainless steel, specimen type B S355 low carbon steel). [Colour figure can be viewed at wileyonlinelibrary.com]

models used in the procedure for each specimen type used the same initial mesh, selected on the basis of convergence studies based on crack configuration factor Y [25].

The models used assumed two perpendicular planes of symmetry, as shown in Figure 5a. When a crack occurs at a single notch intersection, this symmetry assumption is no longer strictly

TABLE 2 | Preloads and working cyclic loads ($R = 0$) for specimen types A and B.

	Preload kN	Working force amplitude kN	Maximum working nominal stress MPa	Maximum working cross-section stress MPa	Theoretical stress concentration factor
Specimen A	21	7.5, 8, 8.5, 9	234.375, 250, 265.625, 281.25	76.53, 81.63, 86.73, 91.83	2.365
Specimen B	75	21, 22, 23, 24, 25	186.67, 195.56, 204.44, 213.33, 222.22	95.238, 99.77, 104.3, 108.84, 113.38	3.2165

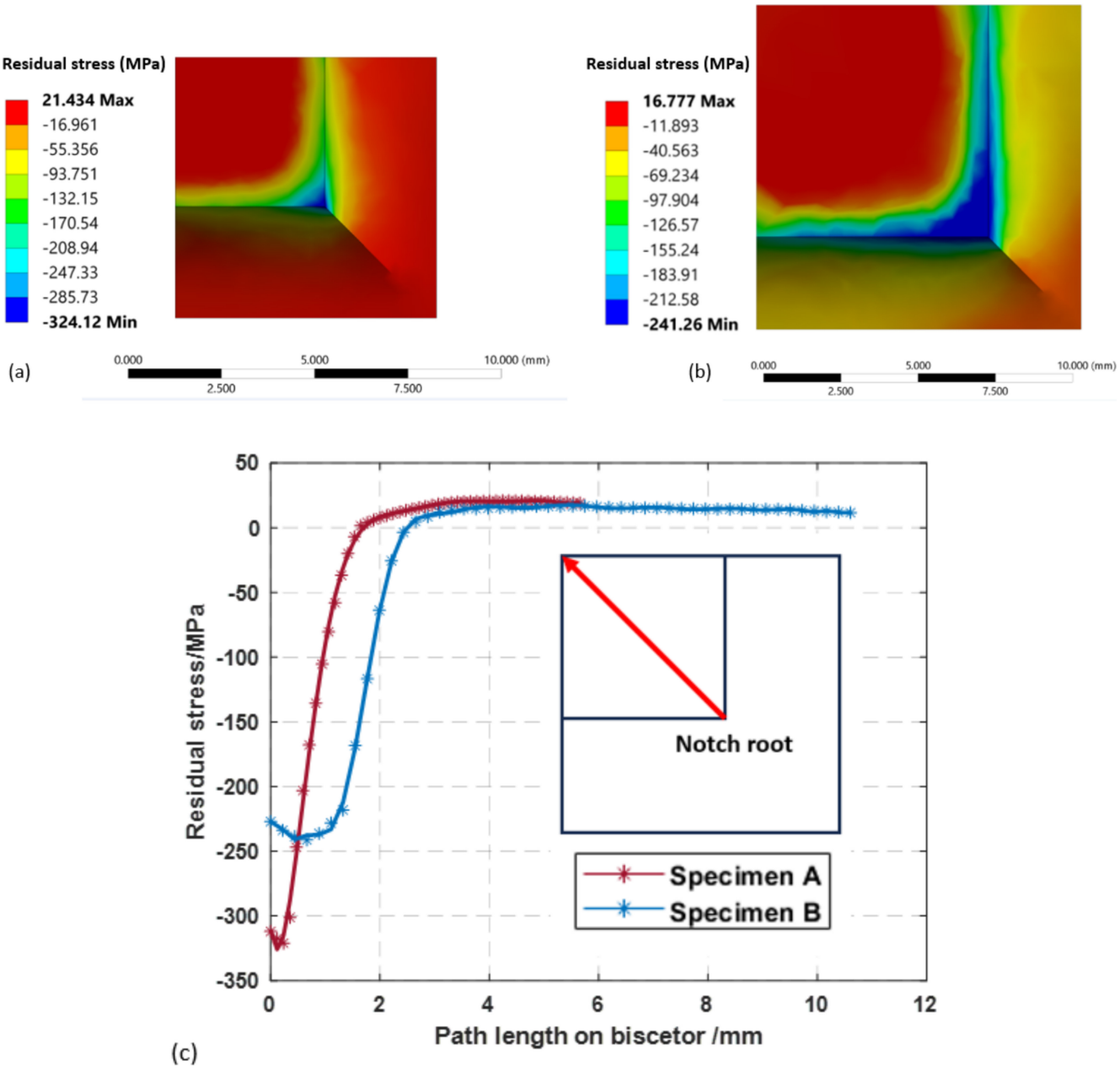

FIGURE 6 | Minimum principal residual stress distribution (MPa) at the notch root for (a) Specimen A and (b) Specimen B. (c) Residual stresses along the bisector. [Colour figure can be viewed at wileyonlinelibrary.com]

valid. However, preliminary investigations of full specimen models showed that the global effect of a crack was negligible for the crack lengths considered here. Plots of the mesh in the notch region for both specimens are shown in Figure 5b. The SMART crack analysis Model 3 assumed a semicircular initial crack of radius 0.2 mm at the notch root.

The quarter-specimen models had symmetry boundary conditions applied on the planes of symmetry and axial displacement set to zero at one end, as shown in Figure 5a. The preload force and working force were evenly distributed over the free end of the model, where the working force varied between zero and a maximum value, $R = 0$. Four different working force levels were considered for Specimen A and five for Specimen B. The preload force and working force amplitude applied to the models correspond to the full specimen test values given in Table 2.

4.3 | Preloading and Residual Stress

Elastic–plastic FEA Model 1 was used to calculate the residual stress field induced in the specimens by initial overloading, using multilinear kinematic hardening material models based on the stress–strain curves of Figure 4. Specimen A is subjected to a preload force of 21 kN to induce local plasticity at the notch root. Upon unloading, local compressive residual stress is induced in this region, balanced by equilibrating tensile residual stress elsewhere in the specimen. Specimen B undergoes the same process with a preload force of 75 kN. The notch region minimum principal residual stress distributions symmetry plane of for both specimens is shown in Figure 6a,b. The residual stress distribution along a line at 45° to the corner on the same plane of symmetry is shown in Figure 6c.

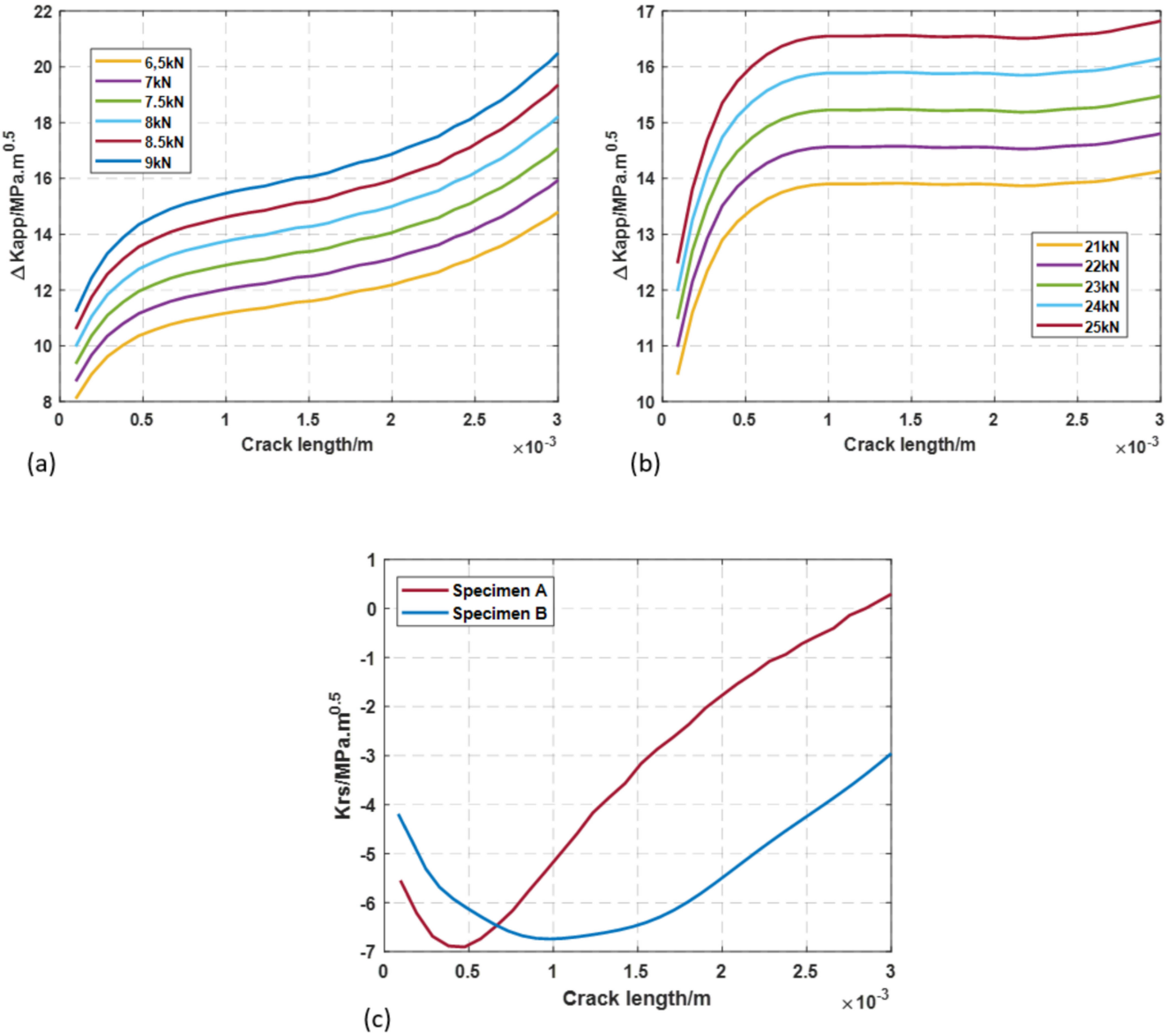

FIGURE 7 | Variation of applied load SIF range ΔK_{app} with increasing crack length for (a) Specimen A and (b) Specimen B. (c) Variation of residual stress SIF K_{rs} with crack length a. [Colour figure can be viewed at wileyonlinelibrary.com]

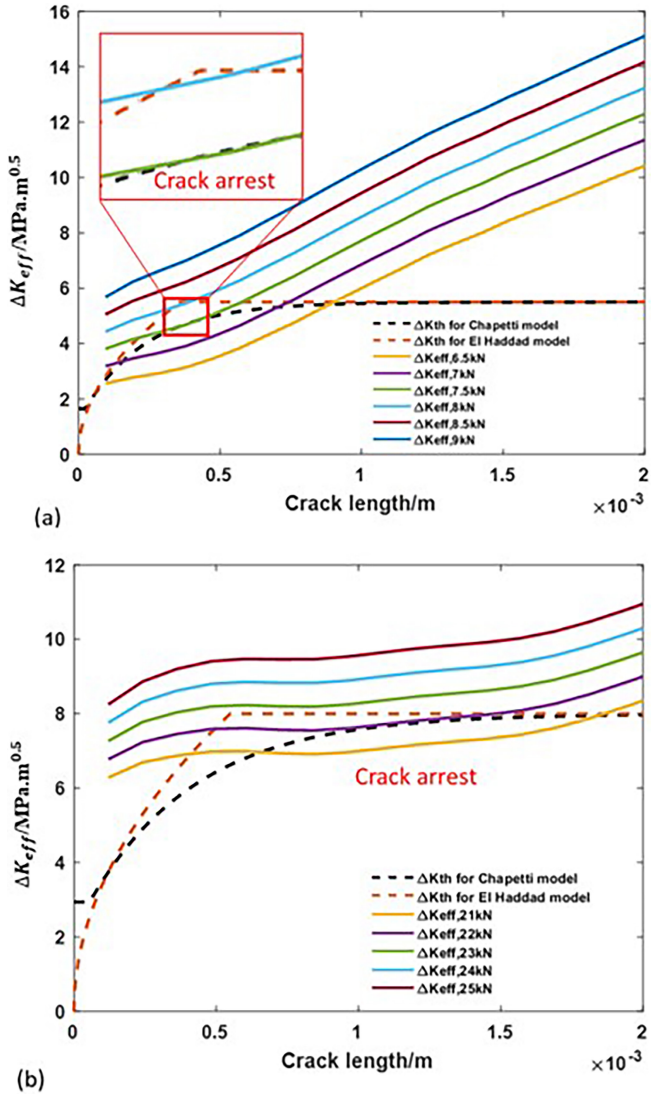

FIGURE 8 | Calculated ΔK_{eff} compared with ΔK_{th} for the different working force levels considered: (a) Specimen A and (b) Specimen B. [Colour figure can be viewed at wileyonlinelibrary.com]

4.4 | Residual Stress SIF

The values of the applied SIF range and the residual stress intensity, ΔK_{app} and K_{rs}, respectively, are calculated in Model 3, using the ANSYS SMART crack growth modeling tool. The residual stress field is initially imported from Model 1. The repeated working forces from Table 2 are applied to the structure to simulate the crack propagation. As the crack propagates, the residual stress redistributes, and the SMART tool automatically remeshes the model, transferring the results from the previous to the new mesh. The calculated variation of ΔK_{app} with increasing crack length a along the bisector is shown in Figure 7a,b for the working force amplitudes considered.

The residual stress SIF, K_{rs}, is calculated using the superposition method proposed by Xiao et al. [25]. The calculated SIF range is independent of the residual stress field:

$$\Delta K = K_{max} - K_{min} = \Delta K_{app}. \tag{8}$$

However, the stress intensity ratio R_K is dependent on the residual stress. The effective stress ratio $R_{K,eff}$ is defined as follows:

$$R_{K,eff} = \frac{K_{min,app} + K_{rs}}{K_{max,app} + K_{rs}}. \tag{9}$$

When the applied force ratio is zero ($R = 0$),

$$R_{K,eff} = \frac{K_{min}}{K_{max}} = \frac{K_{rs}}{K_{max,app} + K_{rs}} = \frac{K_{rs}}{\Delta K_{app} + K_{rs}}. \tag{10}$$

The SMART crack growth tool cannot directly calculate the residual stress SIF; however, this can be done using a superposition method. The model is first analyzed for an arbitrary external cyclic load (of sufficient magnitude to the model to enable crack propagation) with no residual stress, and the SIF range ΔK_{app} calculated. The analysis is then repeated for

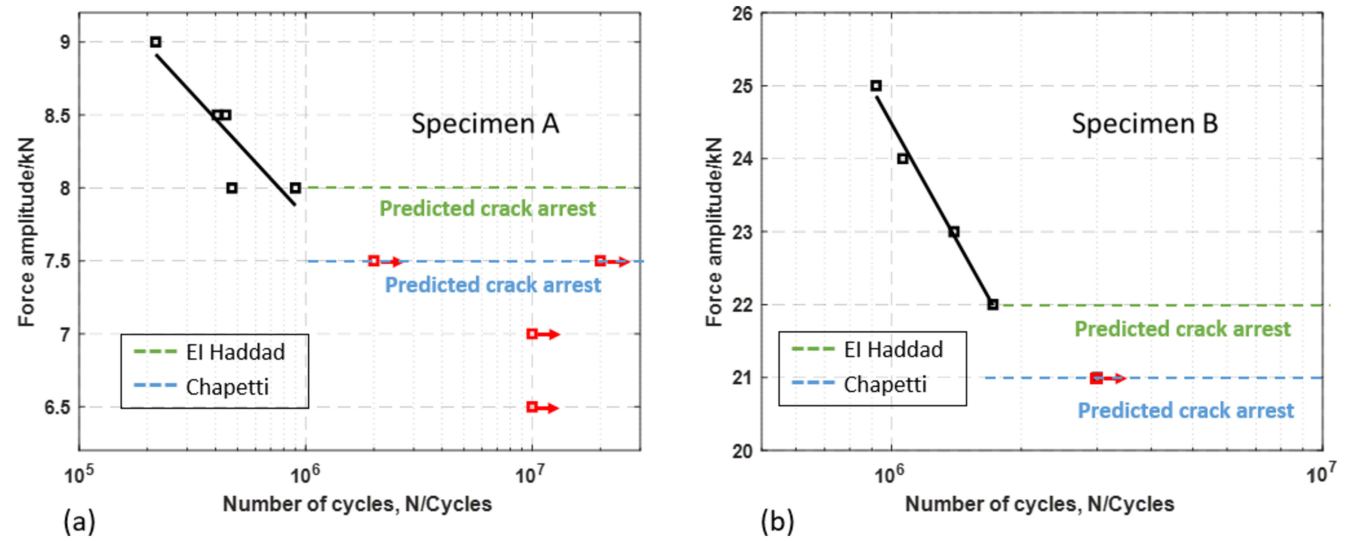

FIGURE 9 | Experimental results of fatigue tests of preloaded double-notched specimens with predicted crack arrest force: (a) Specimen A and (b) Specimen B [22]. [Colour figure can be viewed at wileyonlinelibrary.com]

both the external load and imported compressive residual stress field to determine a combined value of $\Delta K_{app} + K_{rs}$. K_{rs} is then be obtained by superposition, subtracting ΔK_{app} from $\Delta K_{app} + K_{rs}$. The calculated variation of K_{rs} with increasing crack length a is shown in Figure 7c.

4.5 | Effective SIF Range

The plain fatigue limit $\Delta\sigma_{eR}$ and the threshold SIF range ΔK_{thR} used in the calculation of the PSC threshold are defined for stress ratio $R = 0$. However, the effective residual stress ratio $R_{K,eff}$ when residual stress is present varies with crack length.

Elber's crack closure concept [46] proposes that the crack can only propagate when the maximum SIF K_{max} is greater than the crack opening SIF. In this way, only the crack opening part of ΔK plays a role in crack growth. Kujawski [47] proposed that the fatigue crack driving force, K^*, is dependent on both ΔK and K_{max}. Here, K^* is taken as the effective SIF range, ΔK_{eff}. Thus, applying Walker mean stress correction, ΔK_{eff} is given by the following:

$$\Delta K_{eff} = \frac{\Delta K}{(1-R_K)^{\alpha}} \quad for R_K > 0 \tag{11}$$

$$\Delta K_{eff} = \frac{\Delta K}{(1-R_K)} \quad for R_K < 0. \tag{12}$$

4.6 | Crack Arrest Assessment

The El Haddad (2) and Chapetti (4) fatigue threshold models for 316L and S355 determined from the material properties of Table 1 are shown in Figure 8, where ΔK_{th} for the Chapetti model assumes $Y = 0.65$. As a PSC develops from a MSC, crack arrest will occur if the effective SIF range ΔK_{eff} for a given crack length a is below the fatigue crack threshold ΔK_{th}. The effective SIF range for Specimens A and B can be determined from the numerical results for ΔK_{app}, K_{rs} and $R_{K,eff}$, ΔK_{eff} calculated from (11) and (12) by replacing ΔK with ΔK_{app} and R_K with $R_{K,eff}$ for zero-based applied pressures.

The threshold and effective SIF ranges for Specimens A and B are plotted against crack length a in Figure 8a,b, respectively, for each working load level considered. For Specimen A, the maximum force at which crack arrest occurs is 8.0 kN for the El Haddad model and 7.5 kN for the Chapetti model. For Specimen B, the El Haddad model predicts crack arrest for forces 21 and 22 kN. The Chapetti model predicts crack arrest for force 21 kN, but at 22 kN, the effective SIF range is marginally outside the crack arrest boundary.

Test results for fatigue cycles to failure for Specimen A from the experiments [25], with additional data not previously reported in red, and Specimen B [22] are summarized in Figure 9a,b respectively. The results for Specimen A show a finite fatigue life for an applied working force of 8 kN and above. This shows that crack arrest does not occur at 8 kN, as predicted using the El Haddad model. Test results corresponding to the Chapetti model prediction of crack arrest at working load 7.5 kN show run-out at 2×10^6 and 2×10^7 cycles. Specimen B results show finite fatigue life for working force of 22 kN and above, showing that crack arrest does not occur at 22 kN as predicted using the El Haddad model. A single test corresponding to the Chapetti prediction of crack arrest at 21 kN shows run-out at 3×10^6 cycles.

Comparison with fatigue test results indicates that the El Haddad model does not give a conservative estimate of crack arrest within the framework of the proposed method. However, the results given by the Chapetti model indicate that it is a potentially viable approach, within the limits of the run-out data available.

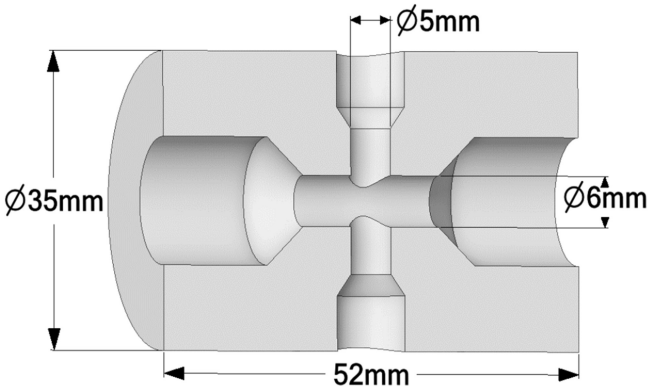

FIGURE 10 | Geometry of half of the valve body [34].

5 | Valve Body Analysis

Sellen et al. [34] presented a stress life design procedure for autofrettage of the complex 3D aluminum AW-6082-T6 valve body shown in Figure 10, validated through experimental observation. Their proposed criterion for required autofrettage pressure is crack arrest under post-autofrettage working loads. They proposed that a conservative condition for this to occur is the maximum post-autofrettage SIF under working loads is always $K_{max} \leq 0$, and the definition of SIF, this condition is satisfied if the corresponding maximum stress normal to the crack plane is always $\sigma_N \leq 0$.

Sellen et al. considered an operational pressure range from 0 to 87.5 MPa, and three autofrettage pressures: 180, 270, and

TABLE 3 | Collected mechanical properties of AW-6082-T6.

Material	σ_y (MPa)	E (GPa)	E_T (MPa)	$\Delta\sigma_{eR}$ $(R = 0)$ (MPa)	ΔK_{thR} $\left(\text{MPa}\sqrt{\text{m}}\right)$	d_1 (μm)	d_2 (mm)	ΔK_{dR} $\left(\text{MPa}\sqrt{\text{m}}\right)$	k $\left(\text{mm}^{-1}\right)$
6082-T6	371	76.5	843	150	2.184	32.3	0.215	0.982	6.325

350 MPa. Experimental analysis showed that crack arrest did not occur for 180-MPa autofrettage, but the observed crack growth suggested that the effective SIF range was close to the threshold value. The 270-MPa autofrettage test was stopped after 10^6 cycles, at which very small cracks were observed. A similar observation was made for autofrettage pressure 350 MPa.

Crack arrest in the valve body of Sellen et al. [34] is analyzed here using the procedure of Figure 1, and the same material properties, material models, and boundary conditions used in FEA are defined by Sellen et al. [34]. Considering the double notch specimen analysis results, the Chapetti model was selected for assessment of crack arrest.

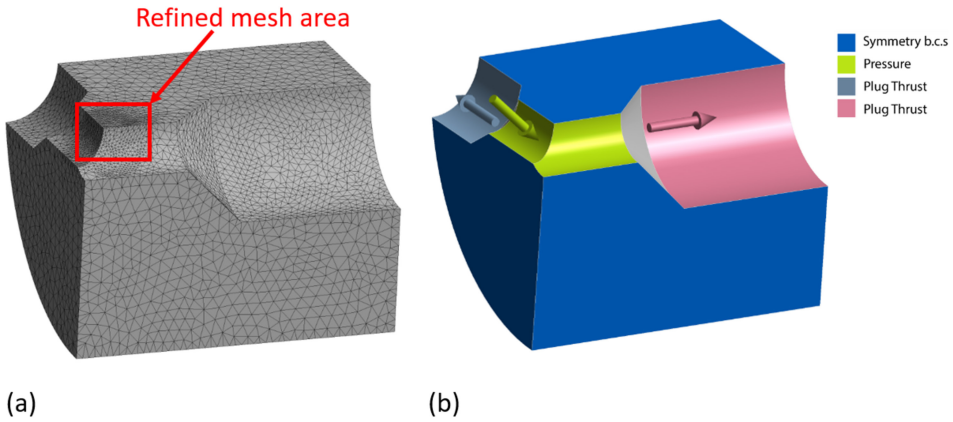

FIGURE 11 | (a) Finite element mesh and (b) applied boundary conditions for 1/8 valve body model. [Colour figure can be viewed at wileyonlinelibrary.com]

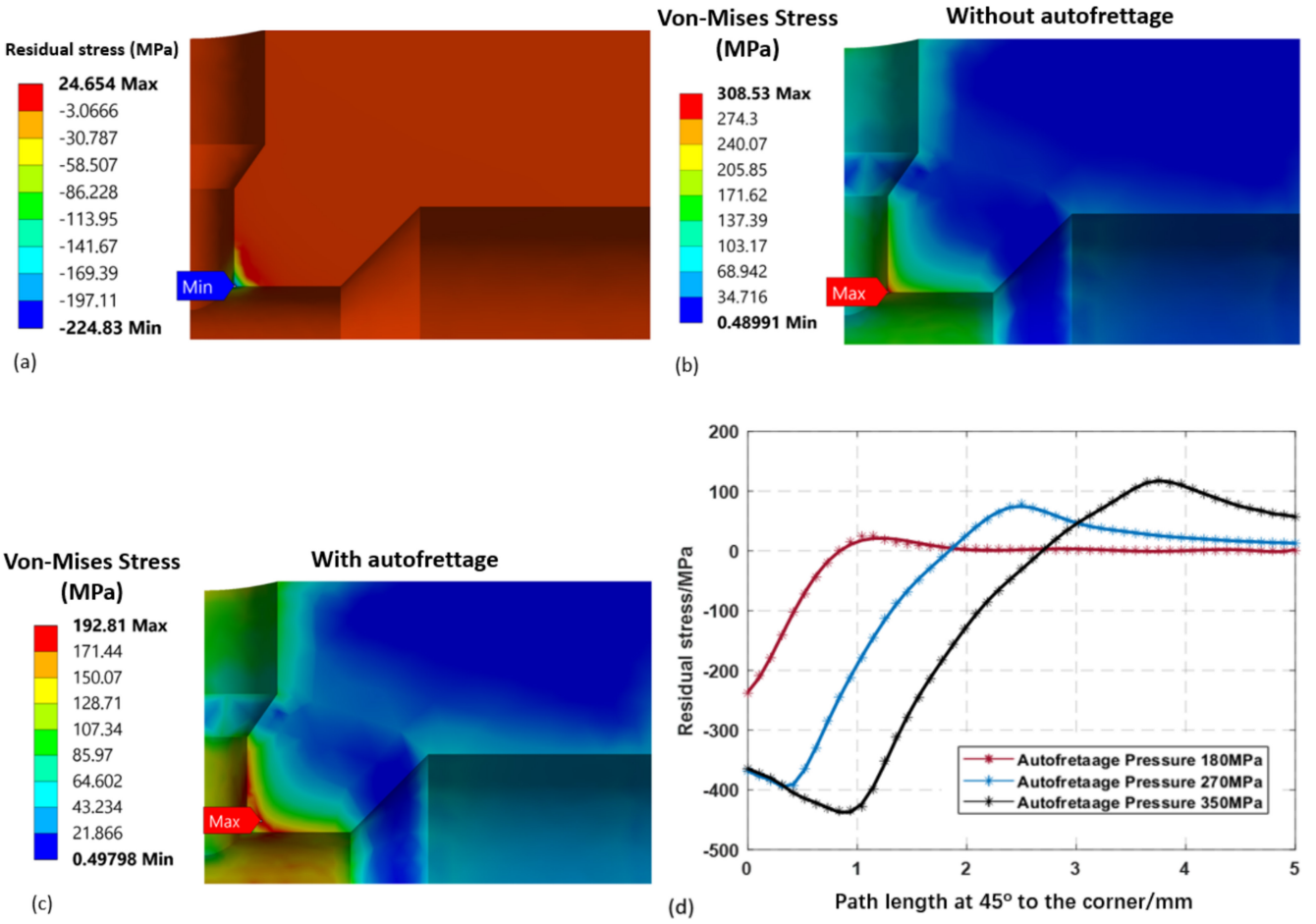

FIGURE 12 | (a) Residual stress normal to the symmetry surface at cross-hole intersection after 180-MPa autofrettage. (b) von Mises equivalent stress distribution at maximum operating pressure 87.5 MPa without autofrettage and (c) with autofrettage pressure. (d) Residual stress along a line at 45° to the corner. [Colour figure can be viewed at wileyonlinelibrary.com]

5.1 | Material Properties

The material properties used in the FEA and crack propagation threshold model obtained from the literature are given in Table 3. Following Sellen et al. [34], the valve body material is assumed to be bilinear kinematic hardening. In constructing the Chapetti model, the value of $\Delta\sigma_{eR}$ was determined from SN curves from the literature [48–50], the value of ΔK_{thR} was obtained from experimental data from the literature [51, 52], and the average grain size was collected from Li et al. [53]. The parameters of Chapetti fatigue threshold model for AW-6082-T6 calculated by (5)–(7) are shown in Table 3.

5.2 | Finite Element Models

The valve body was modeled in ANSYS Workbench using SOLID 187 tetrahedral structural solid elements. The crack-free component has three planes of symmetry, and the monotonic and cyclic stress analysis stages of the assessment procedure can be performed for a 1/8 model with appropriate symmetry boundary conditions. However, if crack initiation occurs on a symmetry plane, the material on both sides of the plane must be modeled when applying ANSYS SMART and a 1/4 model is required.

To obtain the location of crack initiation, 1/8 of the valve body was meshed as shown in Figure 11a. The applied boundary conditions are shown in Figure 11b. Symmetry boundary conditions are applied on the three symmetry planes. The real component is sealed by plugs at the smaller diameter end of the conical transition section of the cross-holes. Pressure was applied to the surfaces within the seal, and the pressure force acting on the plugs was represented by axial thrust forces acting on the larger bores.

Results from cyclic stress analysis shown in Section 5.4 indicate that the crack forms on the horizontal symmetry surface of Figure 11. A 1/4 model with a similar mesh density was therefore created for crack growth analysis, with similar boundary conditions including symmetry boundary conditions, pressure, and plug thrust. The valve was analyzed for an operating pressure cycle from 0 to 87.5 MPa and six autofrettage pressures: 150, 160, 170, 180, 185, and 190 MPa.

5.3 | Preloading and Residual Stress

Elastic–plastic FEA Model 1 was used to calculate the residual stress field induced in the autofrettage process, assuming a bilinear kinematic hardening material model based on material properties of Table 3. The distribution of residual stress normal to the symmetry plane for autofrettage pressure 180 MPa is shown in Figure 12a. The von Mises equivalent stress distribution at the cross-bore intersection for a valve body without autofrettage at maximum operating pressure 87.5 MPa is shown in Figure 12b. The maximum von Mises equivalent stress occurs on the surface at the intersection between the cross-holes. When the valve body has previously experienced autofrettage, the value and location of the maximum von Mises stress can change. Figure 12c shows the von Mises equivalent stress distribution at operating pressure 87.5 MPa for a valve body previously subjected to 180-MPa autofrettage pressure. In this case, the maximum von Mises stress occurs internally, close to the cross-hole intersection. The residual stress distribution along a line at 45° to the corner on the same plane of symmetry is shown in Figure 12d.

5.4 | Crack Location

In a 3D structure with a multiaxial stress field, the location of crack initiation, or critical point, is identified using a multiaxial

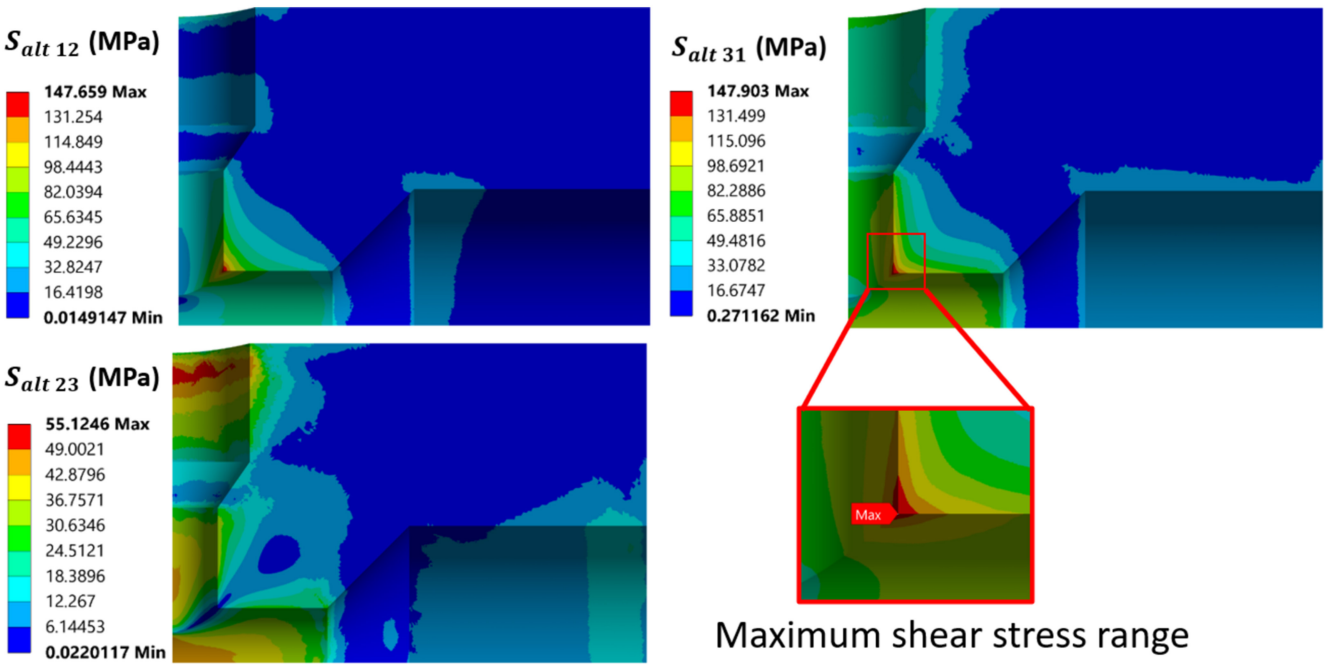

FIGURE 13 | Contour plots of alternating stress $S_{alt\ ij}$ MPa. [Colour figure can be viewed at wileyonlinelibrary.com]

fatigue criterion. Several such criteria, based on both stress and strain, have been proposed. In the critical plane approach [54–56], fatigue failure is dependent on the maximum shear stress range over the load cycle and the mean stress normal to the shear plane [57]. The location of crack initiation and orientation of the crack plane are determined by considering the stress cycle at specific nodes in the model. Depending on the FEA software used, this may be done for all nodes through postprocessor load case calculations, application of internal macros, or exporting stress results to an external program for further processing. At each node, the maximum shear stress plane is identified by the maximum shear stress range between the minimum and maximum loads. This may be defined in terms of principal stress if the principal directions do not change over the load range. If the principal directions change over the cycle, calculation should be based on stress component range. The principal stress differences at a node are as follows:

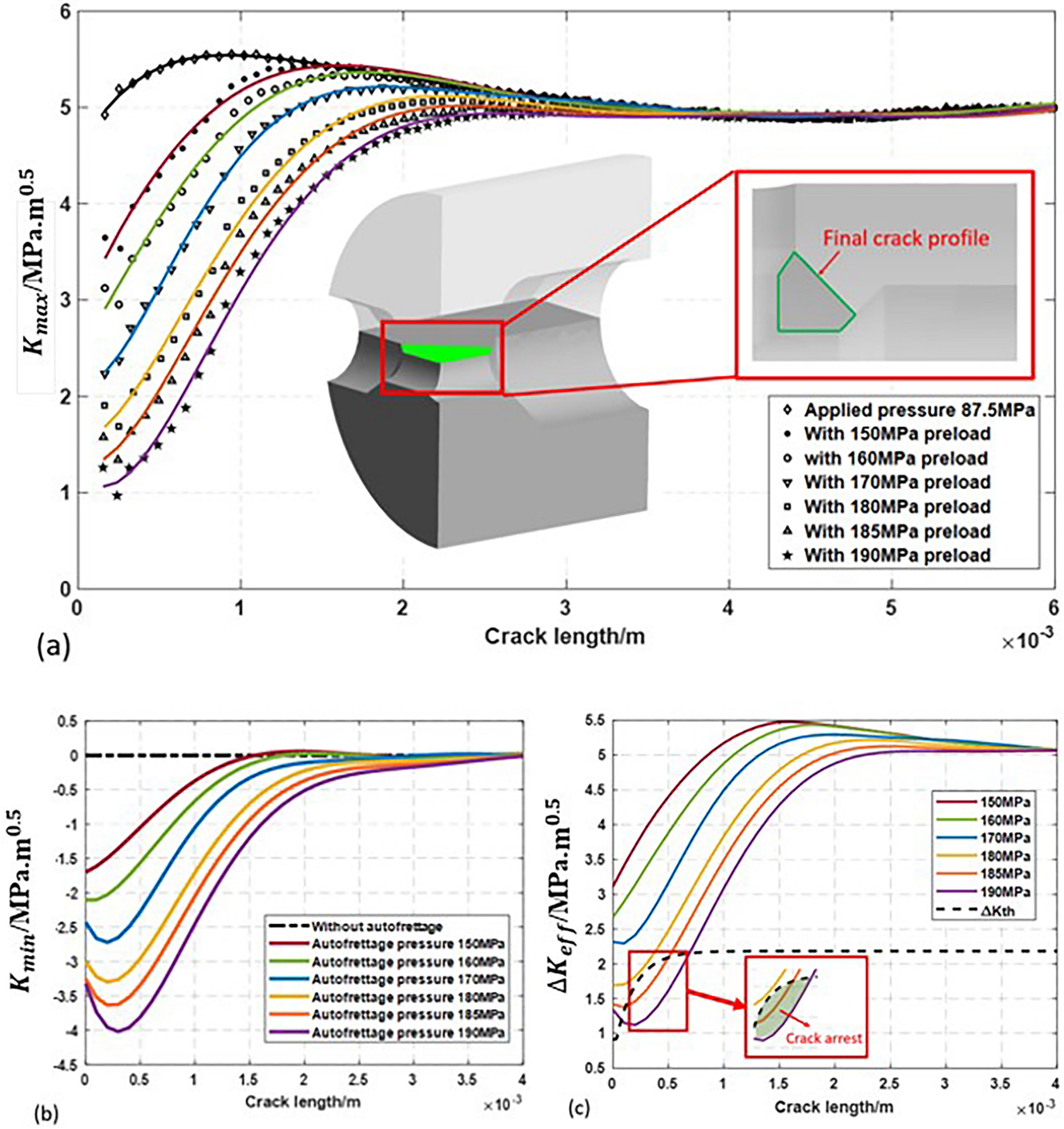

FIGURE 14 | (a) Variation in K_{max} with crack length under working pressure for six autofrettage conditions. (b) Variation in K_{rs} with crack length after autofrettage, with the residual stress normal to the crack plane inset. (c) Comparison of ΔK_{eff} with ΔK_{th}. [Colour figure can be viewed at wileyonlinelibrary.com]

$$S_{12} = \sigma_1 - \sigma_2$$
$$S_{23} = \sigma_2 - \sigma_3. \quad (13)$$
$$S_{31} = \sigma_3 - \sigma_1$$

An alternating shear stress range $S_{alt\ ij}$ ($i \neq j = 1, 2, 3$) is defined for each stress difference, and the maximum alternating stress range at each node was determined as follows:

$$S_{alt\ ij} = max\left[0.5\left(S_{ij\ max} - S_{ij\ min}\right)\right]. \quad (14)$$

Contour plots of the alternating shear stress in the valve body with autofrettage are shown in Figure 13. The highest value occurs for $S_{alt\ 31}$, on the surface at the cross-hole intersection, highlighted in Figure 13. This is therefore defined as the crack initiation location. The crack plane is also defined by the principal stress directions, such that the crack surface corresponds to the plane where the alternating shear stress is $S_{alt\ 31}$. This is in agreement with experimental observation [34].

5.5 | Crack Growth Simulation

An initial semicircle crack was inserted in the quarter model at the identified crack initiation site. The crack plane lies on the X-Z plane. Crack propagation analysis was performed using the ANSYS SMART crack growth tool. Crack growth analysis was performed for six models under cyclic working pressure range 0 to 87.5 MPa ($R = 0$), one with no residual stress and others with initial residual stress corresponding to autofrettage pressures of 150, 160, 170, 180, 185, and 190 MPa imported from elastic–plastic analysis. The calculated variation in K_{max} with increasing crack length along the bisector for each model is shown in Figure 14a, where the final crack profile illustration represents termination of the simulation.

Figure 14a shows that at shorter crack lengths, with the compressive residual stress region, K_{max} decreases significantly with increasing autofrettage pressure. As the crack propagates through the residual stress region, K_{max} approaches a similar value for all the autofrettage conditions considered and beyond the compressive stress zone, after around 3 mm, there is little difference in the curves. A similar response is found for the variation in K_{min} (which is equal to K_{rs} when the minimum applied pressure is zero) with crack length, as shown in Figure 14b. Within the residual stress region, K_{min} decreases significantly with increasing autofrettage pressure, but the curves approach a similar value as the crack grows beyond this.

5.6 | Crack Arrest Assessment

The values of ΔK_{eff} with different autofrettage pressures calculated by (11) and (12) are compared with the Chapetti threshold SIF range ΔK_{th} in Figure 14c. As the autofrettage pressure increases from 150 to 180 MPa, the ΔK_{eff} curves approach the threshold curve, but crack arrest is not predicted. Crack arrest did not occur for autofrettage pressure 180 MPa in the experimental investigation [34], but, based on the form of notch cracks observed in the failed test piece, it was presumed that the effective SIF range was close to the threshold value. This presumption was investigated here by considering the slightly higher autofrettage pressure of 185 MPa. Figure 14c shows that the ΔK_{eff} curve for 185 MPa crosses the Chapetti crack propagation threshold boundary, indicating crack arrest in the PSC region.

6 | Conclusion

This paper presents a new methodology for determining the autofrettage pressure required to achieve crack arrest and hence theoretical infinite fatigue life in pressure components subject to varying working pressure. A high cycle fatigue life assessment framework based on a fracture mechanics crack growth model and FEA [25] is augmented by a crack arrest threshold model to determine the conditions required for crack arrest.

The residual stress distribution due to autofrettage is simulated by elastic–plastic analysis and exported as an initial stress state to a crack propagation model. The residual stress SIF, K_{rs}, is determined by application of a superposition method and FEA crack growth analysis, which is simpler to apply to complex 3D problems than the classical weight function approach. The crack initiation location and crack growth plane orientation are determined by a multiaxial critical plane approach, based on shear stress amplitude. The value of the applied pressure SIF range, ΔK_{app}, for different working pressures is calculated using the ANSYS SMART facility, employing a polynomial equation [25] fit to the SIF-crack length data to reduce computational time for multiple load levels.

The condition for crack arrest was investigated for the two crack propagation threshold models of El Haddad and of Chapetti for MSC, PSC, and LC. The condition for crack arrest is determined by comparing the effective SIF of a growing crack for given autofrettage and working pressures with the calculated crack threshold boundaries. The validity of the method was assessed through analysis of double notch tensile specimens with induced compressive residual stress and comparison experimental fatigue life data. It was found that

- The El Haddad model did not result in a conservative estimate of the required preload for crack arrest.
- The Chapetti model satisfied the necessary condition for crack arrest based on limited run-out experimental data. These data alone are not sufficient to state that crack arrest occurred, and further experimental investigation is required.

The proposed methodology was then applied to a more complex problem, a 3D aluminum valve housing, for which autofrettage test results were available in the literature [34]. The results simulated for a range of autofrettage pressures and fixed working pressure range showed were found to be consistent with the experimentally observed behavior:

- No crack arrest for the minimum autofrettage pressure considered in the experimental study.

- Crack arrest at a slightly higher autofrettage pressure, which agrees with the reported experimental observation that the form of notch cracks at the minimum autofrettage pressure, suggested that the effective SIF range was close to the threshold value.

Overall, comparison of crack arrest analysis using the proposed method with test results for double notch and valve body structures indicates that the method is a promising tool for defining the minimum autofrettage pressure required for crack arrest and hence theoretical infinite fatigue life. Alternatively, the methodology can also be used to determine the autofrettage pressure required to achieve a specific finite fatigue life.

Nomenclature

a	crack length
d_1	the transition between MSC and PSC
d_2	the transition between PSC and LC
E	Young's modulus
E_T	tangent modulus
K^*	fatigue crack driving force
K_{max}	maximum stress intensity factor
$K_{max,app}$	maximum applied stress intensity factor
K_{min}	minimum stress intensity factor
$K_{min,app}$	minimum applied stress intensity factor
K_{rs}	stress intensity factor for the residual stress field
k	parameter used to fit the curve of the PSC regime
L	length of double notch specimens
R	stress ratio associated to the plain fatigue limit amplitude
R_K	stress intensity ratio
$R_{K,eff}$	effective stress intensity ratio
$S_{alt\ ij}$	alternating shear stress range
S_{ij}	stress difference
W	width of double notch specimens
Y	configuration factor
α	correlation parameter
$\sigma_1, \sigma_2, \sigma_3$	principal stresses
σ_a	stress amplitude
σ_{ar}	equivalent stress amplitude
σ_f	plain fatigue limit amplitude
σ_{rs}	residual stress
σ_N	normal stress
σ_y	yield stress
ΔK	stress intensity factor range
ΔK_{app}	range of applied stress intensity factor
ΔK_{dR}	intrinsic threshold
ΔK_{eff}	effective stress intensity factor range
ΔK_{th}	fatigue crack propagation threshold
$\Delta K_{th,a}$	fatigue crack threshold for PSC
ΔK_{thR}	fatigue crack threshold for LC
$\Delta \sigma_{eR}$	plain fatigue limit
$\Delta \sigma_{th}$	endurance limit stress range
FEA	finite element analysis
LCs	long cracks
LEFM	linear elastic fracture mechanics
MSCs	microstructurally short cracks
PSCs	physically short cracks
SIF	stress intensity factor
SMART	Separating Morphing and Adaptive Remeshing Technology
SN	stress number of cycles to failure

Data Availability Statement

The data that support the findings of this study are available from the corresponding author upon reasonable request.

References

1. E. De los Rios, A. Walley, M. Milan, and G. Hammersley, "Fatigue Crack Initiation and Propagation on Shot-Peened Surfaces in A316 Stainless Steel," *International Journal of Fatigue* 17, no. 7 (1995): 493–499.

2. A. Parker, G. O'Hara, and J. Underwood, "Hydraulic Versus Swage Autofrettage and Implications of the Bauschinger Effect," *Journal of Pressure Vessel Technology* 125, no. 3 (2003): 309–314.

3. W. Zhuang and B. Wicks, "Multipass Low-Plasticity Burnishing Induced Residual Stresses: Three-Dimensional Elastic-Plastic Finite Element Modelling," *Proceedings of the Institution of Mechanical Engineers, Part C: Journal of Mechanical Engineering Science* 218, no. 6 (2004): 663–668.

4. A. Chahardehi, F. P. Brennan, and A. Steuwer, "The Effect of Residual Stresses Arising From Laser Shock Peening on Fatigue Crack Growth," *Engineering Fracture Mechanics* 77, no. 11 (2010): 2033–2039.

5. H. Li, R. Johnston, and D. Mackenzie, "Effect of Autofrettage in the Thick-Walled Cylinder With a Radial Cross-Bore," *ASME Journal of Pressure Vessel Technology* 132, no. 1 (2010): 011205.

6. E. Herz, O. Hertel, and M. Vormwald, "Numerical Simulation of Plasticity Induced Fatigue Crack Opening and Closure for Autofrettaged Intersecting Holes," *Engineering Fracture Mechanics* 78, no. 3 (2011): 559–572.

7. V. Okorokov, D. MacKenzie, and Y. Gorash, "Fatigue and Corrosion Fatigue Life Assessment With Application to Autofrettaged Parts," *Proceedings of the Asme 2018 Pressure Vessels and Piping Conference* (USA: American Society of Mechanical Engineers, 2018), V005T10A021.

8. M. Vormwald, T. Schlitzer, D. Panic, and H. T. Beier, "Fatigue Strength of Autofrettaged Diesel Injection System Components Under Elevated Temperature," *International Journal of Fatigue* 113 (2018): 428–437.

9. A. P. Parker, "Autofrettage of Open-End Tubes—Pressures, Stresses, Strains, and Code Comparisons," *Journal of Pressure Vessel Technology* 123, no. 3 (2001): 271–281.

10. H. Jahed, B. Farshi, and M. Hosseini, "The Actual Unloading Behavior Effect on Thermo-Mechanical Stress Intensity Factor and Life of Autofrettage Tubes," *International Journal of Fatigue* 29, no. 2 (2007): 360–369.

11. H. Mughrabi, B. Donth, and G. Vetter, "Low-Temperature Autofrettage: An Improved Technique to Enhance the Fatigue Resistance of Thick-Walled Tubes Against Pulsating Internal Pressure," *Fatigue and Fracture of Engineering Materials and Structures* 20, no. 4 (1997): 595–604.

12. D. Rees, "A Bounding Method for Predicting the Fatigue Life of Plain and Autofrettaged Thick-Walled Cylinders," *International Journal of Fatigue* 13, no. 1 (1991): 59–67.

13. A. P. Parker and J. H. Underwood, "Stress Intensity, Stress Concentration, and Fatigue Crack Growth Along Evacuator Holes of Pressurized, Autofrettaged Tubes," *Journal of Pressure Vessel Technology* 118, no. 3 (1996): 336–342.

14. E. A. Badr, J. R. Sorem, Jr., and S. M. Tipton, "Evaluation of the Autofrettage Effect on Fatigue Lives of Steel Blocks With Crossbores Using

a Statistical and a Strain-Based Method," *Journal of Testing and Evaluation* 28, no. 3 (2000): 181–188.

15. S.-I. Lee and S.-K. Koh, "Residual Stress Effects on the Fatigue Life of an Externally Grooved Thick-Walled Pressure Vessel," *International Journal of Pressure Vessels and Piping* 79, no. 2 (2002): 119–126.

16. M. Pölzl and J. Schedelmaier, eds., "Fatigue Strength Curves of Thick Walled Tubes Under Consideration of Autofrettage," in *ASME 2003 Pressure Vessels and Piping Conference. High Pressure Technology: Shaping High Pressure Technology for the Future* (Cleveland, Ohio, USA: ASME, 2003), 85–90.

17. R. Thumser, J. Bergmann, E. Herz, O. Hertel, and M. Vormwald, "Variable Amplitude Fatigue of Autofrettaged Diesel Injection Parts," *Materialwissenschaft und Werkstofftechnik: Entwicklung, Fertigung, Prüfung, Eigenschaften und Anwendungen Technischer Werkstoffe* 39, no. 10 (2008): 719–725.

18. S. Sellen, S. Maas, T. Andreas, P. Plapper, A. Zürbes, and D. Becker, "Improved Design of Threaded Connections by Autofrettage in Aluminium Compounds for Cyclic High Pressure Loading: Design Calculations and Experimental Verification," *Fatigue and Fracture of Engineering Materials and Structures* 38, no. 6 (2015): 714–729.

19. H. Jahed, B. Farshi, and M. Hosseini, "Fatigue Life Prediction of Autofrettage Tubes Using Actual Material Behaviour," *International Journal of Pressure Vessels and Piping* 83, no. 10 (2006): 749–755.

20. N. E. Dowling, K. S. Prasad, and R. Narayanasamy, *Mechanical Behavior of Materials: Engineering Methods for Deformation, Fracture, and Fatigue* (UK: Pearson, 2013).

21. J. Alegre, P. Bravo, and M. Preciado, "Design of an Autofrettaged High-Pressure Vessel, Considering the Bauschinger Effect," *Proceedings of the Institution of Mechanical Engineers, Part E: Journal of Process Mechanical Engineering* 220, no. 1 (2006): 7–16.

22. V. Okorokov, D. MacKenzie, Y. Gorash, M. Morgantini, R. van Rijswick, and T. Comlekci, "High Cycle Fatigue Analysis in the Presence of Autofrettage Compressive Residual Stress," *Fatigue and Fracture of Engineering Materials and Structures* 41, no. 11 (2018): 2305–2320.

23. H. Bueckner, "Weight Functions for the Notched Bar," *ZAMM-Journal of Applied Mathematics and Mechanics/Zeitschrift für Angewandte Mathematik und Mechanik* 51, no. 2 (1971): 97–109.

24. K. Guo, R. Bell, and X. Wang, "The Stress Intensity Factor Solutions for Edge Cracks in a Padded Plate Geometry Under General Loading Conditions," *International Journal of Fatigue* 29, no. 3 (2007): 481–488.

25. X. Xiao, V. Okorokov, and D. Mackenzie, "High Cycle Fatigue Life Assessment of Notched Components With Induced Compressive Residual Stress," *International Journal of Pressure Vessels and Piping* 206 (2023): 105069.

26. Y. E. Ma, P. Staron, T. Fischer, and P. E. Irving, "Size Effects on Residual Stress and Fatigue Crack Growth in Friction Stir Welded 2195-T8 Aluminium–Part II: Modelling," *International Journal of Fatigue* 33, no. 11 (2011): 1426–1434.

27. O. Doğan, C. Yuce, and F. Karpat, "Effects of Rim Thickness and Drive Side Pressure Angle on Gear Tooth Root Stress and Fatigue Crack Propagation Life," *Engineering Failure Analysis* 122 (2021): 105260.

28. A. Ignatijev, B. Nečemer, J. Kramberger, and S. Glodež, "Fatigue Crack Initiation and Propagation in a PM-Gear Tooth Root," *Engineering Failure Analysis* 138 (2022): 106355.

29. Y. F. Lee and Y. Lu, "Advanced Numerical Simulations Considering Crack Orientation for Fatigue Damage Quantification Using Nonlinear Guided Waves," *Ultrasonics* 124 (2022): 106738.

30. H. Yu and M. Kuna, "Interaction Integral Method for Computation of Crack Parameters K–T–A Review," *Engineering Fracture Mechanics* 249 (2021): 107722.

31. X. Xiao, V. Okorokov, and D. Mackenzie, "High Cycle Fatigue Analysis With Induced Residual Stress Based on Fracture Mechanics," *Procedia Structural Integrity* 52 (2024): 111–121.

32. M. H. El Haddad, K. N. Smith, and T. H. Topper, "Fatigue Crack Propagation of Short Cracks," *Journal of Engineering Materials and Technology* 101, no. 1 (1979): 42–46.

33. M. D. Chapetti, "Fatigue Propagation Threshold of Short Cracks Under Constant Amplitude Loading," *International Journal of Fatigue* 25, no. 12 (2003): 1319–1326.

34. S. Sellen, S. Maas, T. Andreas, P. Plapper, A. Zürbes, and D. Becker, "Design Rules for Autofrettage of an Aluminium Valve Body," *Fatigue and Fracture of Engineering Materials and Structures* 39, no. 1 (2016): 68–78.

35. H. Kitagawa, "Applicability of Fracture Mechanics to Very Small Cracks or the Cracks in the Early Stage," in *Proceedings of 2nd ICM* (Cleveland, 1976), 627–631.

36. J. Araújo and D. Nowell, "Analysis of Pad Size Effects in Fretting Fatigue Using Short Crack Arrest Methodologies," *International Journal of Fatigue* 21, no. 9 (1999): 947–956.

37. A. de Pannemaecker, S. Fouvry, and J. Buffiere, "Reverse Identification of Short–Long Crack Threshold Fatigue Stress Intensity Factors From Plain Fretting Crack Arrest Analysis," *Engineering Fracture Mechanics* 134 (2015): 267–285.

38. M. D. Chapetti and L. F. Jaureguizahar, "Fatigue Behavior Prediction of Welded Joints by Using an Integrated Fracture Mechanics Approach," *International Journal of Fatigue* 43 (2012): 43–53.

39. C. Santus and D. Taylor, "Physically Short Crack Propagation in Metals During High Cycle Fatigue," *International Journal of Fatigue* 31, no. 8–9 (2009): 1356–1365.

40. U. Zerbst, M. Madia, B. Schork, et al., *The IBESS Approach for the Determination of the Fatigue Life and Strength of Weldments by Fracture Mechanics Analysis. Fatigue and Fracture of Weldments* (Germany: Springer, 2019).

41. R. Thumser, J. W. Bergmann, and M. Vormwald, "Residual Stress Fields and Fatigue Analysis of Autofrettaged Parts," *International Journal of Pressure Vessels and Piping* 79, no. 2 (2002): 113–117.

42. K. Tanaka and Y. Akiniwa, "The Cyclic R-Curve Method for Predicting Fatigue Crack Growth Threshold Based on Modified Strip-Yield Model of Plasticity-Induced Crack Closure Under Fully Reversed Loading," *Engineering Fracture Mechanics* 284 (2023): 109194.

43. K. Mohammad, A. Ali, B. Sahari, and S. Abdullah, eds., "Fatigue Behavior of Austenitic Type 316L Stainless Steel," in *IOP Conference Series: Materials Science and Engineering* (UK: IOP Publishing, 2012).

44. M. Wang, Y. Bu, Z. Dai, and S. Zeng, "Characterization of Grain Size in 316L Stainless Steel Using the Attenuation of Rayleigh Wave Measured by Air-Coupled Transducer," *Materials* 14, no. 8 (2021): 1901.

45. M. Abdel-Karim, "Effect of Elastic Modulus Variation During Plastic Deformation on Uniaxial and Multiaxial Ratchetting Simulations," *European Journal of Mechanics - A/Solids* 30, no. 1 (2011): 11–21.

46. W. Elber, "The Significance of Fatigue Crack Closure," in *Damage Tolerance in Aircraft Structures* (USA: ASTM International, 1971), p. 0.

47. S. Dinda and D. Kujawski, "Correlation and Prediction of Fatigue Crack Growth for Different *R*-Ratios Using K_{max} and ΔK^{+} Parameters," *Engineering Fracture Mechanics* 71, no. 12 (2004): 1779–1790.

48. D. Jíša, P. Liškutín, T. Kruml, and J. Polák, "Small Fatigue Crack Growth in Aluminium Alloy EN-AW 6082/T6," *International Journal of Fatigue* 32, no. 12 (2010): 1913–1920.

49. J. Lukács, Á. Meilinger, and D. Pósalaky, "High Cycle Fatigue and Fatigue Crack Propagation Design Curves for 5754-H22 and 6082-T6 Aluminium Alloys and Their Friction Stir Welded Joints," *Welding in the World* 62 (2018): 737–749.

50. D. Siebert and C. Radlbeck, "Experimental Investigation of the Effect of Different Static Mechanical Properties and Inclined Welding on the Fatigue Strength of Welded Aluminum Details," *Engineering Proceedings* 43, no. 1 (2023): 48.

51. L. Borrego, J. Ferreira, and J. Costa, "Fatigue Crack Growth and Crack Closure in an AlMgSi Alloy," *Fatigue and Fracture of Engineering Materials and Structures* 24, no. 4 (2001): 255–265.

52. T. Mann, "The Influence of Mean Stress on Fatigue Crack Propagation in Aluminium Alloys," *International Journal of Fatigue* 29, no. 8 (2007): 1393–1401.

53. D.-f. Li, X.-j. Wang, and Z.-l. Zhao, "Grain Orientation and Texture Analysis of 6082 Aluminum Alloy Friction Plug Welded Joints," *Journal of Materials Research and Technology* 18 (2022): 1763–1771.

54. C. Wang and M. Brown, "On Plastic Deformation and Fatigue Under Multiaxial Loading," *Nuclear Engineering and Design* 162, no. 1 (1996): 75–84.

55. J. Li, Z.-p. Zhang, Q. Sun, and C.-w. Li, "Multiaxial Fatigue Life Prediction for Various Metallic Materials Based on the Critical Plane Approach," *International Journal of Fatigue* 33, no. 2 (2011): 90–101.

56. D. Gao, W. Yao, W. Wen, and J. Huang, "A Multiaxial Fatigue Life Prediction Method for Metallic Material Under Combined Random Vibration Loading and Mean Stress Loading in the Frequency Domain," *International Journal of Fatigue* 148 (2021): 106235.

57. ASME, "ASME Boiler and Pressure Vessel Code Division 3." A*lternative Rules for High Pressure Vessels,* (New York USA, 2015).